Experimental determination of the surface photometric contribution in the spectral reflectance deconvolution processes for a simulated martian crater-like regolithic target

Aurélien M. Cord [*], Patrick C. Pinet, Yves Daydou, Serge D. Chevrel

Laboratoire de Dynamique Terrestre et Planétaire (UMR5562/CNRS/Université Paul Sabatier), Groupe de Recherche de Géodésie Spatiale, Observatoire Midi-Pyrénées, 14, Av. Edouard Belin, 31400 Toulouse, France

Abstract

We produce bidirectional reflectance experimental measurements in the visible and near-infrared range of a macroscopic target simulating the case of a martian crater. Using Hapke's equation of radiative transfer, we compare the performance, in terms of mineralogical abundance determination, of different deconvolution processes on a multispectral image of the experimental target. In particular, we study the effects of the topography and the physical properties of natural rocky surfaces (e.g., local variations of incidence and emergence angles, grain size variations, mixtures of materials) on the data interpretation. For this purpose, we increase progressively the amount of quantitative knowledge available in terms of Hapke parameters description, textural properties and topography for the target. We estimate the accuracy of results in comparison with the known ground truth as a function of the level of knowledge we have of the target and carry out a critical assessment on the relative applicability of the different processes. This study shows that the more important parameters to take into account are (in decreasing order): (1) the textural roughness which is shown essential for the accurate determination of mineralogical abundances; (2) the disparity of Hapke parameters across the target (3) the topography (DEM) that has a limited influence on the results. These findings have obvious implications for interpreting planetary regolith reflectance properties in terms of photometry, spectroscopy and mineralogy, measured either from spaceborne (e.g., Io observations from Galileo, Mars from Mars-Express/HRSC and OMEGA) or in situ (Mars Pathfinder, MER) instruments.

1. Introduction

The planetary surfaces can be seen as a mixture of many different minerals. When interpreting remote sensing reflectance data, one of the key objectives is to quantify and map the mineralogy of planetary materials. However, it is difficult to apply a deconvolution process, which provides an accurate estimate of the mineral abundances as it depends greatly on mixture in a pixel and the correct choice of the mixing model. This arises from the fact that the reflectance spectra depend in a complex manner on (1) the properties of the individual components comprising the surface (absorption coefficients, phase function), (2) the physical state of the surface (particle size, surface roughness) and (3) the observation conditions. Several theories based on the scattering principles exist (Chandrasekhar, 1960; Van de Hulst, 1980; De Haan et al., 1987; Stamnes et al., 1988; Mishchenko et al., 1999; Shkuratov and Helfenstein, 2001). Among them, Hapke (1981, 1986, and 1993) developed an approximate analytical solution, which provides the bidirectional reflectance of a particulate medium, using the radiative transfer equation describing the multiple scattering of light from soils. It is a nonlinear function of the single

[*] Corresponding author. Fax: +33-5-61-33-29-00.
E-mail addresses: aurelien.cord@cnes.fr, acord@rssd.esa.int (A.M. Cord).

scattering albedo and parameters linked with the geometric conditions of observations, the multiple scattering, the phase function, the opposition effect and the roughness.

Depending on the scale of the distribution of the materials within the pixel, we may consider two kinds of mixture, either areal or intimate (Poulet et al., 2002; Poulet and Erard, 2004). For areal or macroscopic mixtures, the reflectance spectrum of a pixel can be considered as a linear combination of some spectra derived from small areas representing distinct materials (called "endmembers") chosen within the image or extracted from a spectral library: a Spectral Mixing Analysis (SMA) can be applied (Adams et al., 1986; Roberts et al., 1998; Chabrillat et al., 2000). In this approach, the spectral properties of the endmembers are combined linearly in a least-squares mixing algorithm to provide the best fit for each pixel. For intimate or "salt and pepper" mixtures, the mean single scattering albedo of a particulate mineral mixture is a linear combination of the single scattering albedo of the components, weighted by the cross sectional area of each component (Hapke, 1981; Johnson et al., 1983). An established method to handle the deconvolution process is to calculate the single scattering albedo image, using photometric modeling (such as the Hapke model) and then perform a SMA. This method is widely applied on experimental spectra (Mustard and Pieters 1987, 1989; Johnson et al., 1992; Sabol et al., 1992), or on integrated telescopic and spaceborne photometric observations for the study of photometric function of lunar terrains or regolithic soils of asteroids (Helfenstein et al., 1996; Mustard et al., 1998; Li and Mustard, 2000; Tompkins, 2002). Some studies give the comparison of Hapke's model and other methods (Hiroi and Pieters, 1994; Nichols et al., 1999; Cheng and Domingue, 2000; Poulet et al., 2002). These works generally do not take into account the global set of Hapke's parameters as it is not available.

Differently from earlier experimental works dealing with powder mixtures analyzed using laboratory spot spectroscopy (e.g., Mustard and Pieters, 1989; Sabol et al., 1992; Johnson et al., 1992; Hiroi and Pieters, 1994), in which the experiments were designed to minimize any influences on photometric parameters due to variations in particle size, textural roughness and regolith structure, the purpose of the present study is to investigate experimentally the case of a "real-world" extended target and to assess the effect on data interpretation when increasing progressively the amount of quantitative knowledge available in terms of surface composition, textural properties and topographic description for the controlled target. Indeed, this is an attempt at addressing the case of natural surfaces for understanding how to proceed with the deconvolution and interpretation of multispectral and hyperspectral imaging data obtained on rock/soil surfaces in planetary exploration and earth observation.

To carry out such an experiment, we have built up a controlled target, with varied mineralogies at the subpixel scale, simulating a crater modifying the martian surface (Fig. 1). Then we have produced measurements by means of a spec-
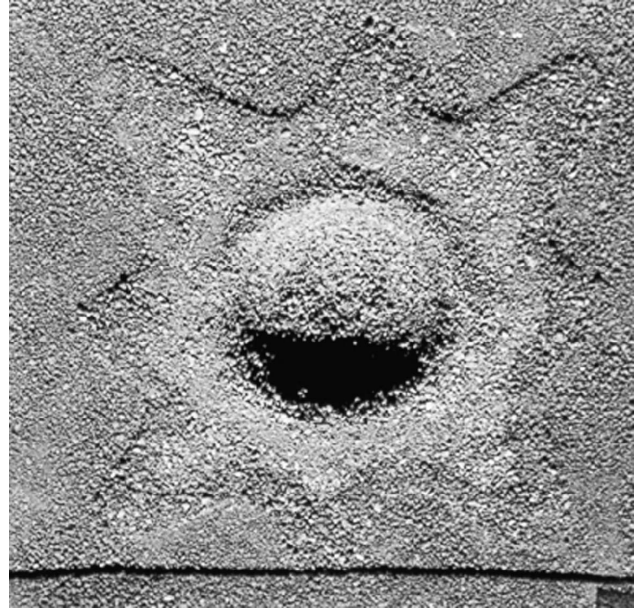

Fig. 1. Photo of the "real-world" target. It simulates a crater modifying the martian surface It sizes about 20 × 20 cm.

tral wide-field imaging facility, at the Midi-Pyrenees Observatory, France, and dedicated to the measurement of the multispectral properties of macroscopic surfaces (20 × 20 cm) with a submillimeter spatial resolution within the 0.40–1.05 µm domain (Pinet et al., 2000, 2001). We compare the performance of different deconvolution processes (linear and nonlinear) applied on a multispectral image of the controlled target.

We first depict the target and the facility used for the measurements and then we describe the methodology (Hapke's model, endmembers research method and spectral mixing analysis). Finally we present and analyze the results from the different deconvolution processes.

1.1. The target

We built a target that is a good simulation of a crater modifying the martian regolith (Fig. 1). We chose this kind of geologic structure because on one hand it is frequently observed on planetary surfaces (Barlow, 2000) and on the other hand it has a complex photometric behavior due to mixtures of minerals, local variations of incidence and emergence angles and grain size distributions. This synthetic target simulates the major photometric variations induced by an impact process, in terms of local topography slopes, inverted stratigraphy and surface redistribution associated with impact ejecta, not regarding the thermodynamic effects due to impact-driven pressure and temperature conditions (e.g., fusion products, glasses). In particular, the geometric aspect ratios of the crater are taken into account in order to best approximate the photometric variations expected in the real case. Since the total target size is about 20 × 20 cm, the simulated crater is 21 mm deep and 80 mm wide in diameter, providing a maximum slope angles about 35° in the

wall of the crater. Figure 2 shows the digital elevation model (DEM) of the target, allowing the evaluation of local incidence and emergence angles for each pixel. The calculation of the DEM is axially symmetric. It is different from the real topography of the target that shows eight distinct lobes of material arranged in a star-shaped pattern. However, the error estimate on the evaluation of incidence and emergence angles for each pixel is less than 4° and this has a minor influence on the deconvolution process results.

The target is composed of three different types of basaltic materials:

- A fresh unaltered basalt, with some phenocrysts of olivine, pyroxene and plagioclase, from a lava flow of Pic d'Ysson (Massif Central, France). This sample is labeled "basalt".
- An oxidized basaltic red-tephra, labeled "tephra", from Flagstaff Cinder Sales (Arizona, USA) containing few phenocrysts of plagioclase. This material is related to explosive-type basaltic volcanism, with some effects of iron oxidation.
- A highly altered basalt, palagonitic-like material, labeled "palagonite", from the Salagou Lake (Herault, France). This basalt has been intensively altered by low temperature water circulation.

The chemical whole rock analyses are given in Table 1. These three selected materials are good analogs of materials existing on planetary surfaces, particularly for Mars (Erard and Calvin, 1997; Murchie et al., 2000). They have varied grain size ranges (see Table 2b). The presence of those large grains induces an important "mesoscopic roughness" as defined in Cord et al. (2003a). Indeed, in this study, it was shown that the submillimetric to centimetric scales influence strongly the optical response. The materials present different spectra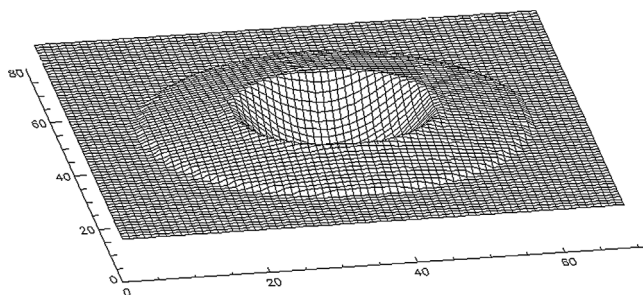l properties (Fig. 3): one is a grey material with no spectral dependence (basalt) while the two others have a high reflectance increasing as a function of wavelength. The red tephra and the palagonite both have a low spectral contrast in order to investigate how effective the deconvolution process is for their discrimination.

A preparatory study detailed in Cord et al. (2003a), allowed us to handle the photometrical properties of the three materials: it presents a method for a determination of the global set of parameters involved in Hapke's model (shown here in Table 2a) when dealing with a set of angular conditions representative of the usual range of observation in planetary exploration for spaceborne optical instruments.

The target comprises three stratigraphic surface layers, illustrated in Fig. 4, with the following sequence from top to bottom: tephra, palagonite and basalt. A fraction of the three layers is distributed in the synthetic ejecta to simulate the inverted stratigraphy. As a result, the target has seven different concentric zones, each having specific compositions from the outermost to the innermost: 100% tephra, 80% tephra and 20% palagonite, 80% palagonite and 20% basalt, 100% basalt, 100% tephra, 100% palagonite, 100% basalt. The materials are intimately mixed in the crater's ejecta and the compositional variability has been produced by controlled volumic mixtures, allowing us to master the reference volumic proportion inside each zone. Then, assuming the composition to be identical for each pixel inside a zone, we compute, for each material, an image giving the expected mineralogical abundance for all the pixels, called ideal Mineralogical Fraction Images (ideal MFI) (Figs. 9a–9c). Due to the volumic control of the mixture, the mineralogical abundances are equivalent to the geometrical
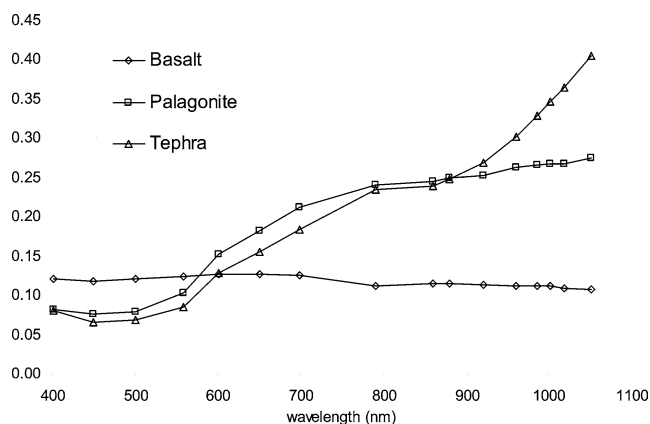

Fig. 3. Bidirectional reflectance factor spectra of the three materials. The incidence angle is 30° and emergence 0°.

Fig. 2. Digital Elevation Model computed for the crater (unit is pixel).

Table 1
Chemical whole rock analyses for the three materials (w%)

	SiO$_2$	Al$_2$O$_3$	Fe$_2$O$_3$	MnO	MgO	CaO	Na$_2$O	K$_2$O	TiO$_2$	P$_2$O$_5$	LOI
Basalt	42.8	11.5	12.9	0.3	15.3	9.6	2.7	1.2	2.1	0.6	1.0
Palagonite	45.8	19.4	7.3	0.1	3.2	5.4	2.2	4.1	0.6	0.2	11.7
Tephra	48.0	17.9	11.8	0.2	5.8	9.7	3.7	0.7	1.7	0.5	0.2

The precision on determination is ±1%.

Table 2
(a) Values of Hapke's parameters for the three materials present in the target sourced from a preparatory study (Cord et al., 2002c), (b) repartition of material grain sizes present in the crater

	(a) Hapke's parameters					(b) Grain sizes	
	b	c	h	B_0	θ	Min. (µm)	Max (µm)
Basalt	0.42	0.32	0.14	0.16	25.0	250	2000
Palagonite	0.44	0.40	0.13	0.25	25.0	50	1000
Tephra	0.41	0.52	0.30	0.15	25.0	50	1000
Mean	0.42	0.44	0.2	0.2	25.0		

The mean values adopted when considering that the parameters are constant across the target are in the last line.
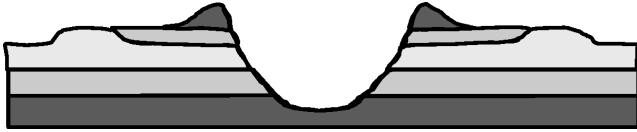

Fig. 4. Organization of three materials in stratigraphic layers, with a sequence from top to bottom of tephra (in light grey), palagonite (in deep grey) and basalt (in black) horizons.

cross-sections of each material. These images will be used as a reference to evaluate the results from the different deconvolution processes. Some errors are produced when we compute the ideal MFI due to grain sizes that are occasionally close to the pixel size. Besides, one should note that our estimates have only a statistical meaning for each zone; however, this is not critical since, in the following, we will focus on the relative performance of tested processes. Despite its relative simplicity, this target allows us to statistically quantify the influence of photometry on unmixing processes.

1.2. Instrumentation

The spectral imaging facility is located at the Midi-Pyrénées Observatory in Toulouse, France (Pinet et al., 2000, 2001; Cord, 2003). It measures the bidirectional reflectance properties of macroscopic targets (about 20 × 20 cm), with a spatial resolution of 0.2 mm per pixel. The measurements are obtained in visible and near-infrared range by means of 16 narrow band interferential filters: their typical band pass is 15 nm and their central wavelengths are ranging from 0.4 to 1.05 µm. We produced a multispectral image of the target with an incidence angle of 30° and an emergence angle of 0°.

The bidirectional reflectance is obtained using a spectralon as a reference during measurements. To account for its non-Lambertian behavior, the spectralon standard used has been calibrated by means of measurements produced by ONERA, Toulouse, France, and consistently compared with independent recent estimates (Bonnefoy et al., 2001).

A 6 × 6 binning is applied on the multispectral image, which both increases the signal to noise ratio (SNR ∼ 200) and smoothes the local heterogeneities at the pixel scale (spatial resolution ∼ 1.2 mm) for the purpose of reducing the target optical complexity (orientation of crystal facet, anisotropy). The homogeneity of the measurements across

the field of view estimated at the pixel scale ranges from 0.005 to 0.01 in reflectance, depending on the considered wavelength (Pinet et al., 2000, 2001). With this binning, we are aware that the pixels are smaller than the largest grain sizes (Table 2b). The validity of the photometric model we use (Hapke) is not well established for observations of individual soil particles. However, the grain size classes are large enough to assume that most of the pixels contain a lot of small particles that are eventually mixed with larger ones. It is valid to take into account the photometric behavior of small particles using Hapke's model. Then, we assume that the model is valid for most of pixels. During the comparison of deconvolution processes results, there is a statistical average coming from the large number of pixels that are present in the image (more than 30,000).

1.3. Method

In the different deconvolution processes used in this paper, the data are expressed in bidirectional reflectance or transformed into single scattering albedo using Hapke's equation (Hapke, 1981, 1986, 1993). In all the cases, each pixel's spectrum of the multispectral image is considered as the result of the mixing of a number of reference material spectra, referred to as the endmembers in the following.

In this section, we give a short description of Hapke's model, endmember research using Principal Components Analysis (PCA) and the spectral mixing analysis.

1.3.1. Hapke's model

Hapke (1993) proposes an empirical model to calculate the bidirectional reflectance (r). Here we rely on what Hapke calls "reflectance coefficient" or "reflectance factor", $R = \pi r / \cos(i)$. This is the usual outcome of laboratory measurements (relative to a reference sample observed under similar geometry):

$$R = \frac{w}{4(\mu_0 + \mu)} \left[\left(1 + B(g)\right) P(g) + H(\mu_0) H(\mu) - 1 \right] S(\theta),$$

(1)

where μ_0, μ are, respectively, the cosines of incidence and emergence angles, g is the phase angle, w is the single scattering albedo, B is the opposition effect function, P is the phase function, H is the isotropic multiple scattering function and S is the function for macroscopic roughness.

The *H* function used is given in Hapke (1993), corresponding to an approximation with a difference of less than 1%.

The double Henyey–Greenstein function, including two parameters, describes the particle phase function $P(g)$ with sufficient accuracy for most radiative transfer calculations in planetary regoliths (McGuire and Hapke, 1995; Hartman and Domingue, 1998):

$$P(g) = (1-c)\frac{1-b^2}{(1+2b\cos(g)+b^2)^{3/2}}$$
$$+ c\frac{1-b^2}{(1-2b\cos(g)+b^2)^{3/2}}, \tag{2}$$

where *b* and *c* are the two parameters linked with the material properties.

With a phase angle of 30°, the coherent backscattering opposition effect (CBOE) is negligible (Helfenstein et al., 1997; Hapke et al., 1998; Shepard and Arvidson, 1999; Kaasalainen et al., 2001; Shkuratov and Helfenstein, 2001). Consequently, only the shadow hiding opposition effect (SHOE) should lightly influence the measurements and is described by the function $B(g)$ in Hapke (1993).

The function for macroscopic roughness $S(\theta, \mu_0, \mu)$, called topographic shadowing function in the following, is presented in Hapke (1993). The parameter θ provides a measure of surface macroscopic roughness inside a pixel. The macroscopic roughness alters the local incidence and emergence angles.

The preparatory study undertaken on the three materials composing the crater (Cord et al., 2003a) gave us typical values, which are presented in Table 2a, for all the parameters involved in Hapke's equations. Moreover, it showed that in the spectral domain under consideration in this study, i.e., 0.4–1.05 microns, the shadowing function and the particle phase function are weakly dependent on the wavelength (Cord et al., 2003b). It is not taken into account here and we consider that Hapke parameters only depend on the physical and mineralogical properties of the selected materials.

1.3.2. Endmember research

The Principal Components Analysis (PCA) takes advantage of both spatial distribution and spectral characteristics (Smith et al., 1985; Johnson et al., 1985). It is a mathematical technique that describes a multivariate set of data using "derived variables." The derived variables are formulated using specific linear combinations of the original variables (in this case, the wavelengths). They are uncorrelated and computed in decreasing order of variance. Therefore PCA constructs a small set of derived variables that reduces the dimensionality of the original data. In this study, the three first axes take into account more than 96% of the variability of our multispectral image. Consequently, for the data representation, all the pixels of the multispectral image, associated to spectra, are projected in the space of the three first axes of PCA, giving a cloud of points. Figure 5 shows,
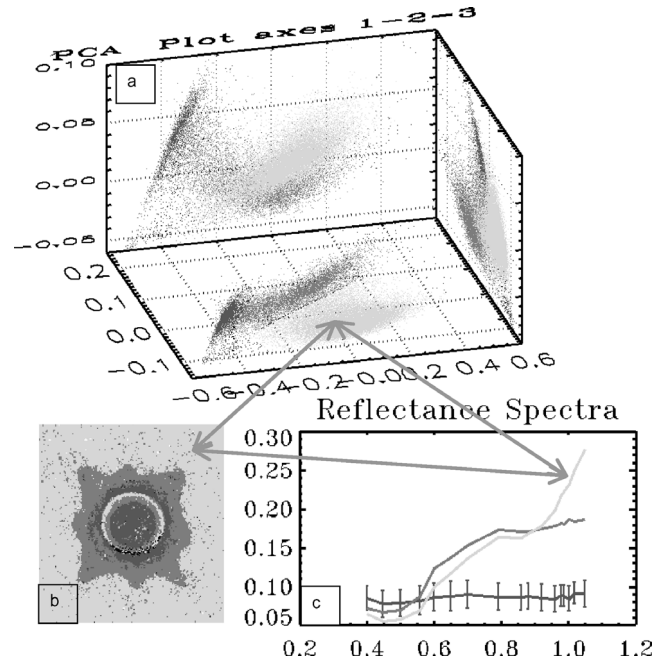

Fig. 5. (a) PCA cloud, (b) image of the target, (c) associated spectra.

for the crater multispectral image, the pixel locations in the PCA clouds associated with both the locations inside the image and the spectra. This approach is used to relate the statistical distribution of the spectral properties within the multispectral dataset with criteria of spatial coherency based on knowledge of the observed scene. It allows an optimal selection of image endmembers generally from the edge of the PCA clouds, representing spectrally extreme pixels. Moreover this method is helpful to depict the mixing trends between the different endmembers of the image in relation to their spatial distribution.

1.3.3. Spectral mixing analysis

Whether the data are in bidirectional reflectance or in single scattering albedo, a number of endmember spectra of known composition are selected as described above. The spectral properties of the endmembers are combined in a least-squares mixing algorithm to provide the best fit for each pixel within the image. Each pixel (i, j) is thus represented by a proportion of each endmember required to minimize the difference between the model spectrum and the actual spectrum:

$$S_{i,j}^{\lambda_l} = \sum_{k=1}^{M} F_{i,j}^k R_k^{\lambda_l} + E_{i,j}^{\lambda_l}, \tag{3}$$

where M: number of endmembers; $S_{i,j}^{\lambda_l}$: measured reflectance of pixel i, j for wavelength λ_l; $F_{i,j}^k$: mixing coefficient of endmember k for pixel i, j; $R_k^{\lambda_l}$: reflectance of endmember k for wavelength λ_1; $E_{i,j}^{\lambda_l}$: error for pixel i, j and wavelength λ_l.

Table 3
Values of criteria applied during the linear spectral mixing analysis to select pixels that are properly modeled

	Mean level	RMS	RMS per wavelength
Bidirectional reflectance data	0.155	0.01	0.015
Single scattering albedo data	0.499	0.02	0.03

Then, the RMS error for each pixel is:

$$\varepsilon_{i,j} = \sqrt{\frac{1}{N}\sum_{l=1}^{N} E_{i,j}^{\lambda_l}{}^2},$$

(4)

where N: number of wavelengths.

The inversion is a minimization of the RMS error for each pixel using different combinations of the endmembers (see Iterative Spectral Mixing Analysis in Chabrillat et al., 2000). Based on the evaluation of the instrument accuracy estimates on the reflectance measurements (cf. Section 1.2), we define the statistical result as the proportion of pixels that have a satisfactory solution according to the following quantitative criteria:

- The relative mixing coefficient for each endmember is constrained between 0 and 1.1.
- The RMS error has to be less than 0.01 for bidirectional reflectance image and 0.02 for single scattering albedo image.
- The absolute error for each wavelength $E_{i,j}^{\lambda_l}$ should be less than 0.015 for bidirectional reflectance image and 0.03 for a single scattering albedo image.

The values used for the different cases (bidirectional reflectance and single scattering albedo) are summarized in Table 3. We notice that the mean level of a bidirectional reflectance image is three times less than the mean level of a single scattering albedo image, explaining the differences between criteria applied.

The outcomes of such analyses are

- Endmember Mixing Coefficient Images (EMCI), representing the proportion of each selected endmembers.
- A standard-deviation image, RMS image, revealing the units that are not satisfactorily described by the proposed model in terms of unexplained residual variance.

In our case, we produce three EMCI, one for each material. To estimate the contribution of shade/shadow from the scene, we compute a relative luminosity image, using the following formula:

$$A_{i,j} = \sum_{k=1}^{M} F_{i,j}^{k}.$$

(5)

The Fig. 6a shows this image for the deconvolution process labeled "const" in the following. It shows the relative luminosity of each pixel in comparison with the mean
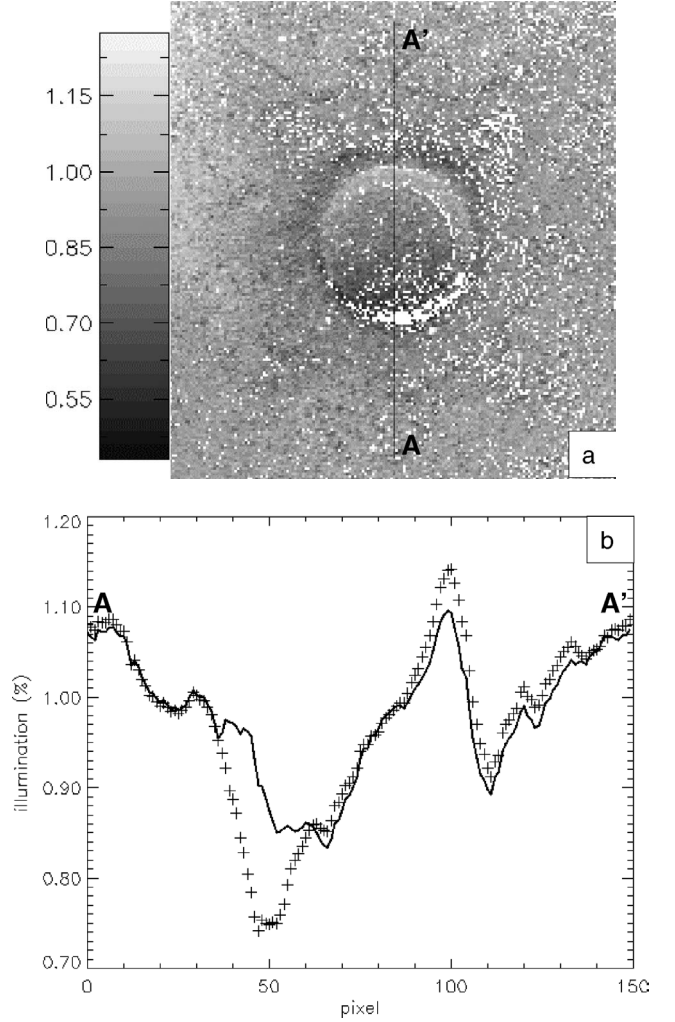

Fig. 6. (a) Luminosity image for the case labeled "const". This image is less than 1 when the pixel luminosity is smaller than the mean luminosity of the endmembers. White pixels are not satisfactorily inverted pixels. (b) A–A′ profile of the illumination images. The crosses correspond to "const" and the line to "dem".

luminosity of the endmembers. The darkest area is located on the wall of the crater, on the side of the light source, as expected. This image derives from the SMA and allows us to take into account the small variations of luminosity in the scene that are not taken into account by photometric models when it is applied before. Relying on the idea that shadow contribution leads to a linear variation on spectra, the EMCI are renormalized by this image in order to eliminate the effects due to shadowing from those related to the nature of the material:

$$\forall i, j, k, \quad \tilde{F}_{i,j}^{k} = \frac{F_{i,j}^{k}}{A_{i,j}},$$

(6)

giving

$$\forall i, j \quad \sum_{k=1}^{M} \tilde{F}_{i,j}^{k} = 1,$$

(7)

where $\tilde{F}_{i,j}^k$ is the relative cross sectional abundance of the mineral represented by the endmember k, in the pixel i, j. We should notice that when the data are expressed in single scattering albedo, the relative cross sectional abundances $\tilde{F}_{i,j}^k$ derived from the spectral mixing analysis are actually not directly mineralogical fractions (from Hapke, 1981). In this framework, the mixing coefficients are actually geometrical cross-sections. However, as explained in Section 1.1, due to the volumic control of the material mixtures, the ideal mineralogical abundances are equivalent to the geometrical cross-sections of each material. In the following, we will call $\tilde{F}_{i,j}^k$ the Mineralogical Fraction Image (MFI) that will be comparable with the ideal MFI defined above (Section 1.1).

2. Results and discussion

We compare in the following the performance of different deconvolution processes on the experimental multispectral image, when we increase gradually the amount of quantitative information available for the target. We estimate their respective efficiency as a function of the level of a priori knowledge available for the target and carry out a critical assessment on their relative applicability.

2.1. The five deconvolution processes

(1) We first applied a linear deconvolution process, labeled "linear", where the SMA is directly applied to the bidirectional reflectance. It is a standard technique used for the processing of remote sensing planetary data in the general case, when no a priori knowledge of the target is available. It is the basic approach only valid in the case of areal mixing.

Then, in the subsequent experiments, relying on a technique proposed by Hapke, the deconvolution proceeds in two steps: an inversion of Hapke's model to convert data from bidirectional reflectance into single scattering albedo, followed by a SMA. To evaluate the other parameters of Hapke's model (b, c, h, B_0 and θ), we used a varied amount of information about the target from one case to the other:

(2) Assuming the knowledge of the mean Hapke parameters (except w) of target materials (cf. Table 2a), we transform the multispectral image into single scattering albedo with all parameters constant across the target. This case, labeled "const" in the following, would be in principle only applicable for a macroscopically flat surface composed of grains with similar photometric properties.

Using the digital elevation model (DEM) (cf. Fig. 2), we evaluate the local incidence and emergence angle for each pixel for the transformation into single scattering albedo. This case, labeled "dem", would be valid for a macroscopically uneven target composed of grains having similar photometric properties.

(4) In the highest level of knowledge, the DEM is taken into account and the Hapke parameters (except w) are calculated, for each pixel from the "linear" deconvolution process, as a linear combination of pure materials parameters, weighted by the abundance of each material. Then the single scattering albedo is evaluated for each pixel. This case, labeled "var", is the most adapted to our target: a macroscopically uneven surface composed of grains having varied photometric properties. The combination of Hapke's parameters is probably highly non linear and we must investigate further how the parameters of mixing should be calculated. However, as a first approximation, we will see that this method gives better results than when the spatial variation of mineralogical properties is neglected.

(5) Finally, we have a particular interest in considering the effect of roughness of the target. This case is the same as number 4, except for the topographic shadowing function which is not taken into account, i.e., $\theta = 0°$. This case, labeled "thet0", would be applicable for a virtual surface without any macroscopic roughness inside each pixel. In principle, it could be approached by extremely flat surfaces only composed of very small grain with sizes of a few microns.

All the tested deconvolution processes are summarized in Table 4.

2.2. Comparison between deconvolution processes

All the deconvolution processes give similar statistical results: the proportion of pixels that have a satisfactory solution according to the quantitative criteria defined above (Section 1.3.3) is between 89 and 91% for all the cases. It provides a control on the validity of the mixture modeling, in particular the choice of endmembers.

Hence, the difference arising between the different processes appears in what we define as the physical criteria: it is evaluated by a comparison between the results of the deconvolution processes (calculated MFI) and the ground

Table 4
Summary of the tested deconvolution processes

	Linear	Const	Dem	Var	Thet0
Conversion into w	No	Yes	Yes	Yes	Yes
Incidence and emergence angles	N/A	Constant	Variable	Variable	Variable
b, c, h, B_0 values	N/A	Constant	Constant	Variable	Variable
θ value	N/A	Const $\neq 0$	Const $\neq 0$	Variable	Zero

truth (ideal MFI, Fig. 9a–c): Fig. 7 shows on the abscissa the percentage error between the calculated MFI and the ideal, and on the *y*-axis, the proportion of physically well-modeled pixels for all three materials. It shows that whatever the error threshold, the deconvolution process results are always sorted in the same order: "var", "const" and "dem", "thet0", "linear" from best to worst. To establish the adequate physical criteria, we rely on the work of Sabol et al. (1992): they use spectral mixture analysis to determine detection limits of target materials in the presence of background materials within the field of view under various compositional conditions. In particular, they show that the detection limit for two materials with low spectral contrast is between 12.5 and 16%. On this basis, we choose an error threshold of 15% and we estimate the followings for each deconvolution process:
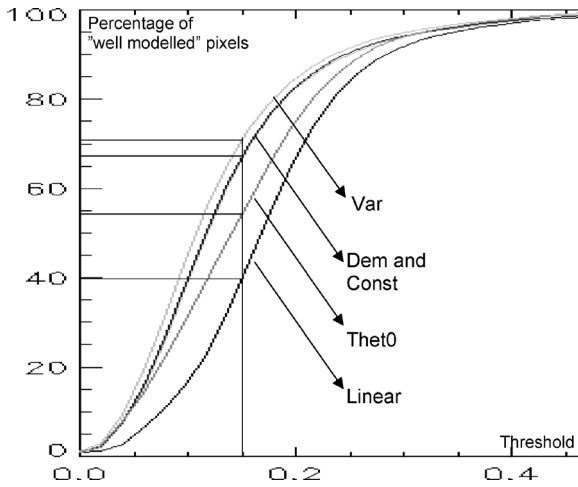

Fig. 7. Cumulated histogram of fitting errors. The threshold is plotted on the abscissa; the percentage of pixels having a difference of less than the threshold between abundance for all three materials and the ideal fractional abundance is plotted on the *y*-axis, for each deconvolution process.

- The percentage of pixels that are physically well modeled according to this threshold (Table 5). It allows a good discrimination between the different deconvolution processes.
- The mean absolute difference between the ideal MFI and the calculated MFI for each material and we obtain Fig. 8.

These indicators show that the physical solutions, provided by the different deconvolution processes, are not equivalent. In the following, we discuss about the dissimilarities.

For instance, Fig. 9 shows also that there are more pixels that have a satisfactory solution according to the quantitative criteria in the darkest part of the center of the crater for the case "linear" than for the case "var". However the mineralogical abundances evaluated in the "linear" case are far from the ground truth (ideal MFI). It illustrates that the best mathematical solution does not correspond to necessarily the best physical solution.

2.2.1. Absolute difference between ideal and calculated MFI

We note that the differences between ideal and calculated MFI, presented in Fig. 8, are large for all the processes: from 8 to 20%. This gap has two main sources: (1) As detailed in

Table 5
Results of deconvolution processes

	Linear	Const	Dem	Var	Thet0
Well modeled	39.7%	66.8%	67.1%	71.1%	54.1%
Mean	0.77	0.83	0.81	0.87	0.81
CV	18.6%	11.7%	8.4%	7.1%	19.4%

The first line correspond to the percentage of pixels that are well modeled for all three materials. The two last to mean and coefficient of variation (CV) of illumination images in the center of the crater.
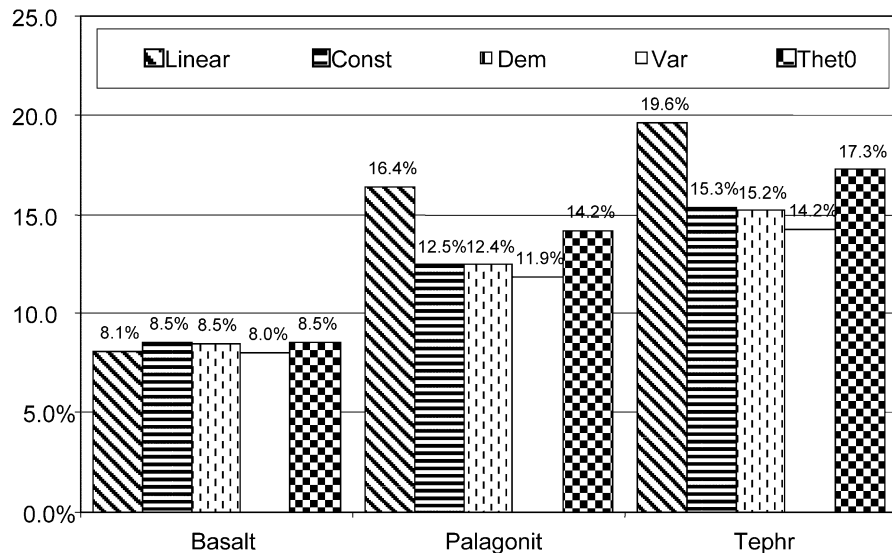

Fig. 8. Mean absolute difference of MFI calculated between the different models and the ideal MFI derived from the ground truth.
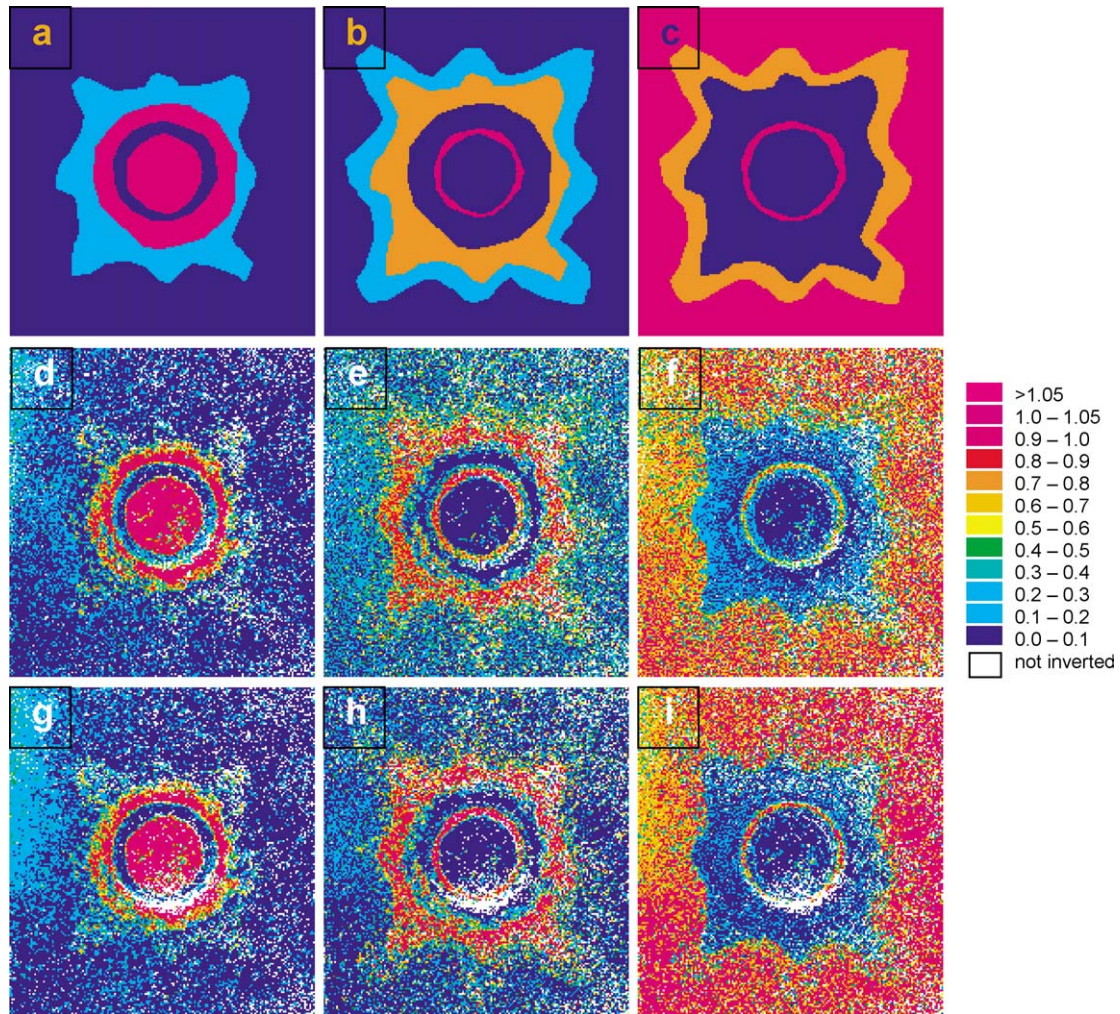
Fig. 9. Mineralogical fraction images (MFI) of basalt, palagonite, tephra from left to the right. (a, b, c) correspond to the ideal MFI derived from the ground truth, (d, e, f) correspond to the "linear" MFI and (g, h, i) correspond to the "var" MFI. White pixels correspond to pixels that have not a satisfactory solution according to the quantitative criteria (Table 5).

Section 1.1, the computation of the ideal MFI is not totally perfect due to the complexity of the target: it is composed of large grain-sized materials (see Fig. 1 and Table 2b), and the composition is not exactly the same from one pixel to another even inside a given zone of expected identical composition. This appears for instance in the calculated MFI of the "linear" process, in the Figs. 9d–9f. Indeed, there are some local variations of the calculated composition, in particular outside of the crater, where the expected composition is 100% of tephra (Fig. 9c). In order to reduce this effect, the hyperspectral image is binned to decrease the spatial resolution up to 1.2 mm/pixel. (2) The large grain-size leads also to variations in the measurements coming from the facet orientations of each grain and from indirect illumination from distant facets. The photometric modeling associated with the deconvolution processes is not able to take into account all this variability. One cannot completely handle the photometric complexity of such a target, and this highlights the need for a better deconvolution process taking into account both

the spectral properties and the spatial connectivity within the target.

However, the absolute difference is not critical here because we focus on the relative performance of the different deconvolution processes.

2.2.2. Difference arising from materials

Figure 8 shows that the physical results, provided by the different deconvolution processes, allow us to distinguish two kinds of materials. For dark materials (basalt), the results are similar for all the models. In contrast, for bright materials (palagonite and tephra), it shows a significant improvement using Hapke's model versus the linear case: a mean absolute difference decrease by more than 4 points. We propose two main reasons for this behavior:

- We saw in Fig. 3 that bright materials have a low spectral contrast and are harder to discriminate from one to each other than the dark material. Therefore, in these cases a more sophisticated model is required.

- The multiple scattering makes a larger contribution to the bidirectional reflectance in the case of bright materials, so considering it through a photometric modeling in the deconvolution process leads to a significant improvement on the results.

It should be reminded that the bright materials considered in this study are ice-free rocky materials, not exceeding 0.4 in reflectance. Indeed, for surfaces having an albedo close to 1 (case of sulfur on the surface of Io (e.g., Geissler et al., 2001; Simonelli et al., 2001; Bonnefoy et al., 2001) or icy surfaces), this effect would be amplified and the contribution of the multiple scattering should not be neglected.

2.2.3. Comparison between the bidirectional reflectance linear deconvolution process and the others

Figure 9 shows three sets of MFI: ideal (Figs. 9a–9c), "linear" (Figs. 9d–9f) and "var" (Figs. 9g–9i). In this figure, the most significant difference between those two deconvolution processes appears on the tephra and palagonite abundance maps. As explained above, those materials have a low spectral contrast and we investigate how effective are deconvolution processes for their discrimination. For instance, we first focus on the outermost zone of the target where 100% tephra are expected, corresponding to a dark red color (Fig. 9c): the "var" case (Fig. 9i) exhibits many more pixels with a high proportion of tephra than the "linear" case (Fig. 9f), which shows a significant proportion of palagonite in this zone (Fig. 9e). Another example: in the part of the ejecta being very close to the rim (in orange in the Fig. 9b, third zone from the outermost to the innermost), we designed the target without any tephra material. However the "linear" case detects about 20% tephra in this area, whereas in the same region the "var" case detects no tephra at all as expected. To quantify those results, we consider the Table 5: it shows that the use of Hapke's modeling for the inversion of spectral data improves by a factor of about 1.75 the proportion of well-modeled pixels: the "linear" case gives a proportion of about 40 and 71% for the case "var". The results of the processes "const" and "dem" are about 67% that is significantly greater than the "linear" case. This supports experimentally (Cord et al., 2002a) the method proposed (Hapke, 1981; Johnson et al., 1983), transforming the bidirectional reflectance into single scattering albedo before spectral mixing analysis. This gives a more efficient way of retrieving the fractional abundance of a wide-field target than the basic linear technique.

In the following sections, we analyze what kinds of information about the surface are crucial to conduct a deconvolution process giving good physical results.

2.2.4. What is the influence on the results when the digital elevation model is taken into account?

In the case "const", the geometrical angles are considered constant across the entire scene. In the case "dem", the local incidence and emergence angles are evaluated for each pixel.

Contrary to what is expected, the two cases show about 67% of well modeled pixels (Table 5) suggesting that the use of a digital elevation model does not improve results

In order to understand the effect of the digital elevation model in the deconvolution process, we focus in the luminosity images (Fig. 6). These images, derived from the SMA, allow us to take into account, inside each pixel, the relative luminosity in comparison with the mean luminosity of the considered endmembers. In this way, the effects of the small variation in luminosity in the scene, mainly due to the mutual shadowing, are discarded during the renormalization step of the SMA (see Section 1.3.3).

Figure 6a shows the luminosity image of the case "const". The significant local variations of incidence and emergence angles are concentrated on the wall of the crater, the area where the variations of shadowing by neighboring grains are the most significant. Indeed, the darkest part is located in this area on the side of the light source and the lightest part on the opposite side. This figure shows that during the process "const" the SMA step has taken into account the variations in luminosity existing inside the target to retrieve the mineralogical abundance (MFI).

To compare the luminosity images of the two processes "const" and "dem", we calculate the profile (AA′) through the center of the crater of the luminosity images (Fig 6b). This plot confirms that the albedo variations are more significant in the walls of the crater. It shows that the variation are larger for the case "const" (cross) than for the case "dem" (line) in Fig. 6. In order to quantify this difference, we calculate in Table 5 the coefficient of variation C.V. (standard deviation divided by the mean) of luminosity images in the walls of the crater for all the deconvolution processes. In the case "const", it displays a variation in albedo 50% greater than in the case "dem", showing that:

- Hapke's model is able to handle the shadowing effects if the Digital Elevation Model is present as in the "dem" case. The calculation of the single scattering albedo is then closer to reality than in the case of a plane approximation.
- The SMA step of the deconvolution process compensates for the absence of a digital elevation model, taking into account the variations of albedo due to topography by means of the illumination image, and allows the retrieval of fraction images consistent with the ground truth after the renormalization step.

Indeed, in this specific experiment, with slopes smaller than 35°, incidence angle 30° and emergence 0°, calculations show that differences in the single scattering albedo using or not a digital elevation model are smaller than 3% when the local incidence decreases due to topography and less than 10% when the incidence increases. Pixels corresponding to this last case are located in the darkest area of the image where the SNR drastically decreases, so they do

not satisfy the statistical criteria and therefore are not considered.

This experiment shows that the SMA is able to take into account the minor effects induced by the topography and, then, the use of a digital elevation model does not improve the abundance determination.

2.2.5. The most accurate results of deconvolution processes

The process "var" corresponds to the case where the maximum amount of information about the target is used to transform the bidirectional reflectance into single scattering albedo. So, as expected, it produces the most accurate results among the tested deconvolution processes: it improves by a factor greater than 1.75 the number of well-modeled pixels in comparison with the "linear" case (from 40 to 71%, cf. Table 5). Consequently, this approach should be recommended for interpreting bidirectional reflectance imaging data, either orbital or in situ.

The differences between the results of the other cases using Hapke's model, "const" and "dem", are less significant, but the improvement is not negligible: from 67 to 71% (Table 5). Therefore a good estimation of Hapke's parameters across an extended target ensures the optimum results possible for the deconvolution process and hence provides us with a technique to better model planetary surfaces. It illustrates that the linear combination of Hapke's parameters, weighted by the abundance of each material, is, as a first approximation, an efficient way to estimate locally the parameters. However it opens the door to investigate further how the parameters of mixing should be calculated (Cord et al., 2002b; Stankevich et al., 2002).

In addition, the case "var" has the smallest coefficient of variation within its illumination image (Table 5). In this case, during the computation of the single scattering albedo from the bidirectional reflectance, the effects induced by the mutual shadowing and topography, even inside the pixels, are well controlled by the photometric modeling. This confirms that Hapke's model allows us to better handle the bidirectional reflectance variations due to these effects across the whole target to retrieve a single scattering albedo close to the reality.

2.2.6. Influence of the topographic shadowing function $S(\theta)$

In Hapke's theory, the topographic shadowing function takes into account the effects due to the shadowing inside each pixel and to the local modification of the incident and emission angles. The effect that influences this function results predominantly from an integral of the roughness properties of the surface in the submillimetric to centimetric range inside the pixel of observation: it depends on the surface boundary topography (Helfenstein and Shepard, 1999; Cord et al., 2002b, 2003a; Shkuratov et al., 2005). For our target, composed of grain sizes from 50 μm to 2 mm (Table 2b), this function is dominated by the "rocky" aspect of the surface involving the shape, roughness and topo-

graphic structure of grains. It has obvious implications in the case of regolithic surfaces such as that of Io, as studied by Galileo/SSI instrument, for which θ ranges between 16°and 24° (Geissler et al., 2001; Simonelli et al., 2001). For the lunar regolith, recent results also reveal that the local mare regolith macroscopic roughness ranges between 20° and 26°, with unusual values reaching 35° or more in the case of disturbed surface textures associated with swirls (Pinet et al., 2004). For Mars, in situ observations derived from Viking and Mars Pathfinder photometry (Guinness et al., 1997; Johnson et al., 1999) indicate significant θ variations ranging between 4° and 27°, the rocks being smoother than the soils as a possible consequence of aeolian abrasion and/or coating with atmospheric dust or cemented drifts (McSween et al., 1999) and are consistent with earlier photometric inferences drawn from telescopic observations (e.g., Pinet and Chevrel, 1990; Dolfus and Deschamps, 1993; De Grenier and Pinet, 1995; Martin et al., 1996; Pinet and Rosemberg, 2001). In order to assess the impact of this function $S(\theta)$, we compare a deconvolution process where θ is neglected ("thet0") with the case where it is not ("var"), and all other variables being the same.

Table 5 shows that the result worsens considerably as evidenced by the score of 71% for the case "var" versus 54% for the case "thet0". This result leads to the following conclusions:

(1) It confirms that a surface composed of coarse-grained material has a significant macroscopic roughness effect that strongly influences the bidirectional reflectance measurements.

(2) Neglecting this effect leads potentially to much degraded results in terms of mineralogical prediction. This is supported by illumination images study (Table 5): when neglecting the topographic shadowing function, the variation of the illumination image inside the crater wall is slightly higher (19.4%) than in the linear case (18.6%) and considerably higher than in the non linear cases (between 7.1 and 11.4%). This shows that not taking this effect into account leads to an amplification of the shadowed area during the calculation of the single scattering albedo instead of a reduction as for the non linear cases: then the model is not able to take into account the subpixel shadows existing inside the image and the calculation of the single scattering albedo is incorrect.

(3) The Hapke photometrical model does not account for multiple scattering between elements of large-scale surface topography, which is important for rather bright planetary surfaces. Indeed, improvements of the Hapke theory are very difficult because the rigorous description of shadowing demands numerical calculations, by means of a Monte Carlo ray tracing, for different particulate structures (single-valued topography, rocky or clumpy topography, fractally-arranged topography, e.g., Shepard et al., 2001; Shkuratov and Stankevich, 1992;

Shkuratov and Helfenstein, 2001; Stankevich and Shkuratov, 2000, 2004; Stankevich et al., 1999, 2003). In particular, the domain in which the scale of surface boundary topography is comparable to the size of surface particles has to be investigated more in depth (Cord et al., 2004). However the results of the calculation are too complex to be practical for a deconvolution process. Our experimental results show that, as a first approximation, for noncy material having an albedo less than 0.7, the topographic shadowing function developed by Hapke is able to handle the optical behavior of such a complex surface and to retrieve the material relative mineralogical abundances.

3. Conclusion

This paper addresses several objectives.

First of all, the experiment which has been performed points out the interest of the wide-field multispectral imaging facility set up at the Midi-Pyrénées Observatory for conducting experimental simulations of the optical properties of planetary regolithic surface analogs.

Secondly, we assess the performance of different deconvolution processes relying on Hapke's model of radiative transfer by investigating samples such as natural rock surfaces and bulk soils rather than powder, in order to simulate different textural situations representative of planetary surface states.

Thirdly, we deduce quantified information about linear and nonlinear deconvolution processes applied on a real scene and determine the impacts of target complexities (topography, material mixing, and macroscopic grain size variation) on the bidirectional reflectance spectra interpretation. Relying on the quantitative ground truth available for the built-up target, we compare the results derived from the different processes. We conclude that:

- All the tested processes give similar statistical results: i.e., the proportion of pixels that have a satisfactory solution is between 89 and 91%. However, the determined mineralogical abundances are not identical in all the cases, giving different relative performances in terms of physical appropriateness.
- Compared with the case of the bidirectional reflectance linear spectral mixing analysis, the deconvolution technique proposed by Johnson et al. (1983) provides a method to better quantify and map the mineralogy of a target, whatever are the approximations. The best case is, as expected, the one requiring the largest amount of information. It gives in particular the single scattering albedo closest to the reality.
- The linear combination of Hapke's parameters, weighted by the abundance of each material, is, as a first approximation, an efficient way to estimate locally the parameters. For the inversion of spectral data, it improves

by a factor of 1.75 the proportion of well-modeled pixels with respect to the "linear" case (bidirectional reflectance spectral mixing analysis). However, we must investigate further how the parameters of mixing should be calculated.
- The spectral mixing analysis is able to compensate for the absence of a digital elevation model, i.e., to take into account variations of albedo due to topography.
- The influence of the topographic shadowing function $S(\theta)$ which is predominantly controlled by the roughness properties of the surface boundary topography in the submillimeter to centimeter range is crucial and must be considered for proper mineralogical interpretation.

As a consequence, this study shows that the more important physical parameters to take into account are (in decreasing order): (1) the textural roughness, essential for the accurate determination of mineralogical abundances; (2) the variations per pixel of Hapke parameters across the target and (3) the topography (Digital Elevation Model) that has a limited influence on the results.

Moreover, for ongoing and upcoming orbital spectral data interpretations (e.g., Mars-Express/HRSC and OMEGA instruments; MRO/CRISM), we can suggest a methodology to assure an optimal determination of the subpixel mineralogical abundance: keeping in mind that Hapke parameters of our materials were evaluated using only a limited set of multiangular measurements, our results show that one can derive, from dedicated orbital measurements, the photometric parameters of specific areas representative of the main surface materials. These values should be used for the regional (e.g., Pinet et al., 2004) and global studies of the planetary surfaces and linked with in situ data measured by optical instruments operating on landers or rovers at smaller spatial scales: landscape, rock and even grain scales (e.g., Viking, Guinness et al., 1997; Mars Pathfinder, Geissler et al., 2001; FIDO Prototype Mars Rover Field Trial, Arvidson, 2002; Athena Pancam, Bell et al., 2004, and Microscopic Imager, Herkenhoff et al., 2004). From both types of measurements, the surface physical characteristics could also be extracted (i.e., mesoscale surface roughness, topography) and used for the sake of interpretations.

The future work directions could be to test different sets of Hapke's parameter values (assuming for instance average surface roughness ($\Theta = 15$ or $20°$) and compare the performance of the associate deconvolution processes, to assess the performance of the last developments of Hapke's model (Hapke, 2002) or alternative approaches for radiative transfer models (e.g., Shkuratov et al., 1999; Shkuratov and Helfenstein, 2001; Poulet and Erard, 2004), and to investigate various surface targets in order to simulate different textural situations representative of planetary surface states with a particular emphasis put on the azimuthal effects linked to the occurrence of anisotropic scatterers.

Indeed, new experimental studies are strongly advocated for improving the photometric modeling associated with de-

convolution processes in the case of a complex target. This also highlights the need for improved theoretical modeling to describe the case of natural regolithic surfaces.

Acknowledgments

References

Adams, J.B., Smith, M.O., Johnson, P.E., 1986. Spectral mixture modeling: a new analysis of rock and soil types at the Viking Lander 1 site. J. Geophys. Res. 91 (B8), 8098–8112.

Arvidson, R.E., 2002. Introduction to the special section: FIDO Prototype Mars Rover Field Trial. J. Geophys. Res. 107 (E11), 8001.

Barlow, N.G., 2000. Standardizing the nomenclature of martian impact craters ejecta morphologies. J. Geophys. Res. 105 (E11), 26733–26738.

Bell III, J.F., 24 colleagues, 2004. Mars exploration Rover Athena Panoramic Camera (Pancam) investigation. J. Geophys. Res. 108 (E12).

Bonnefoy, N. 2001. Développement d'un spectrophoto-goniomètre pour l'étude de la reflectance bidirectionnelle des surfaces géophysiques. Application au soufre et perspective pour Io. Thèse de doctorat, Laboratoire de Glaciologie et Géphysique, Univesité Joseph Fourier, Grenoble I.

Chabrillat, S., Pinet, P.C., Ceuleneer, G., Johnson, P.E., Mustard, J.F., 2000. Ronda peridotite massif: methodology for its geological mapping and lithological discrimination from airborne hyperspectral data. IJRS 21 (12), 2363–2388.

Chandrasekhar, S., 1960. Radiative Transfer. Dover, New York.

Cheng, A.F., Domingue, D.L., 2000. Radiative transfer models for light scattering from planetary surfaces. J. Geophys. Res. 105 (E4), 9477–9482.

Cord, A.M. 2003. Hétérogénéité optique et réflectance spectrale des surfaces planétaires solides : études expérimentale et théorique. Thèse de doctorat, Laboratoire de Dynamique terrestre et planétaire, Université Paul Sabatier, Toulouse III.

Cord, A.M., Pinet, P.C., Chevrel, S., Daydou, Y., Shkuratov, Y.G., Stankevich, D.G., Petrov, D.V., 2004. Physical meaning of the Hapke parameter for macroscopic roughness (θ): experimental determination for planetary regolith surface analogs and numerical approach. Lunar Planet. Sci. 35. Abstract 1708. Houston.

Cord, A.M., Pinet, P.C., Daydou, Y., Chevrel, S., 2003a. Planetary regolith surface analogs: optimized determination of Hapke parameters using multiangular spectro-imaging laboratory data. Icarus 165, 414–427.

Cord, A.M., Pinet, P.C., Daydou, Y., Chevrel, S., 2003b. Experimental investigation of the potential wavelength dependence of Hapke parameters in the visible and near infrared range. Lunar Planet. Sci. 34. Abstract 1548. Houston.

Cord, A.M., Pinet, P.C., Daydou, Y., Chevrel, S., 2002a. Influence of linear versus nonlinear mixture on bidirectional reflectance spectra with simulated geologic targets. In: EGS XXVII General Assembly, Nice, France, 21–26 April, 2002. Abstract 1295.

Cord, A.M., Pinet, P.C., Daydou, Y., Stankevich, D., Shkuratov, Yu., 2002b. Planetary regolith surface analogs and mesoscale topograpy: optimized determination of Hapke parameters using multiangular spectro-imaging laboratory data. In: Solar System Remote Sensing Symposium, Pittsburgh, 2002, p. 17.

De Grenier, Pinet, P., 1995. Near-opposition martian limb-darkening: quantification and implication for visible-near infrared bidirectional reflectance studies. Icarus 115, 354–368.

De Haan, J.F., Bosma, P.B., Hovenier, J.W., 1987. The adding method for multiple scattering calculations of polarized light. Astron. Astrophys. 183, 371–391.

Dolfus, A., Deschamps, M., 1993. Soil texture and granulometry at the surface of Mars. J. Geophys. Res. 98 (E2), 3413–3429.

Erard, S., Calvin, W., 1997. New composite spectra of Mars, 0.4–5.7 μm. Icarus 130, 449–460.

Geissler, P., McEwen, A., Phillips, C., Simonelli, D., Lopes, R.M.C., Douté, S., 2001. Galileo imaging of SO_2 frosts on Io. J. Geophys. Res. 106 (E12), 33253–33266.

Guinness, E.A., Ardvidson, R.E., Clark, I.H.D., Shepard, M.K., 1997. Optical scattering properties of terrestrial varnished basalts compared with rocks and soils at Viking Lander sites. J. Geophys. Res. 102 (E12), 28687–28703.

Hapke, B., Nelson, R., Smythe, W., 1998. The opposition effect of the moon: coherent backscatter and shadow hiding. Icarus 133, 89–97.

Hapke, B., 1981. Bidirectional reflectance spectroscopy. 1. Theory. J. Geophys. Res. 86 (B4), 3039–3054.

Hapke, B., 1986. Bidirectional reflectance spectroscopy. 4. The extinction coefficient and the opposition effect. Icarus 67, 264–280.

Hapke, B.W., 1993. Theory of Reflectance and Emittance Spectroscopy. Cambridge Univ. Press, New York.

Hapke, B., 2002. Bidirectional reflectance spectroscopy. 5. The coherent backscatter opposition effect and anisotropic scattering. Icarus 157, 523–534.

Hartman, B., Domingue, D., 1998. Scattering of light by individual particles and the implications for models of planetary surfaces. Icarus 131, 421–448.

Helfenstein, P., Shepard, M., 1999. Submillimeter-scale topography of the lunar regolith. Icarus 141, 107–131.

Helfenstein, P., Veverka, J., Thomas, P.C., Simonelli, D.P., Klaasen, K., Johnson, T.V., Fanale, F., Granahan, J., McEwen, A.S., Belton, M., Chapman, C.R., 1996. Galileo photometry of Asteroid 243 Ida. Icarus 120, 48–65.

Helfenstein, P., Veverka, J., Hillier, J., 1997. The lunar opposition effect: test of alternative models. Icarus 128, 2–14.

Herkenhoff, K.E., 22 colleagues, 2004. Athena Microscopic Imager investigation. J. Geophys. Res. 108 (E12), 8065.

Hiroi, T., Pieters, C.M., 1994. Estimation of grain sizes and mixing ratios of fine powder mixtures of common geologic minerals. J. Geophys. Res. 99 (E5), 10867–10879.

Johnson, P.E., Smith, M.O., Adams, J.B., 1983. A semiempirical method for analysis of the reflectance spectra of binary mineral mixtures. J. Geophys. Res. 88 (B4), 3557–3561.

Johnson, P.E., Smith, M.O., Adams, J.B., 1985. Quantitative analysis of planetary reflectance spectra with Principal Components Analysis, Proc. Lunar Planet. Sci. Conf. 15. J. Geophys. Res. 90, C805–C810. Supplement.

Johnson, P.E., Smith, M.O., Adams, J.B., 1992. Single algorithms for remote determination of mineral abundances and particle size from reflectance spectra. J. Geophys. Res. 97 (E2), 2649–2657.

Johnson, J.R., Kirk, R., Soderblom, L.A., Gaddis, L., Reid, R.J., Britt, D.T., Smith, P., Lemmon, M., Thomas, N., Bell III, J.F., Bridges, N.T., Anderson, R., Herkenhoff, K.E., Maki, J., Murchie, S., Dummel, A., Jaumann, R., Trauthan, F., Arnold, G., 1999. Preliminary results on photometric properties of materials at the Sagan Memorial Station, Mars. J. Geophys. Res. 104, 8809–8830.

Kaasalainen, S., Piironen, J., Muinonen, K., 2001. Oposition effect of regolith-type materials. In: EGS XXVI, General Assembly, Nice, France, 25–30 March.

Li, L., Mustard, J.F., 2000. Compositional gradients across mare-highland contacts: importance and geological implication of lateral transport. J. Geophys. Res. 105 (E8), 20431–20450.

Martin, P.D., Pinet, P.C., Bacon, R., Rousset, A., Bellagh, F., 1996. Martian surface mineralogy from 0.8 to 1.05 microns TIGER spectro-imagery measurements in Terra Sirenum and Tharsis Montes formation. Planet. Space Sci. 44 (8), 859–888.

McGuire, A.F., Hapke, B., 1995. An experimental study of light scattering by large, irregular particles. Icarus 113, 134–155.

McSween, H.Y. Jr., Murchie, S.L., Crisp, J.A., Bridges, N.T., Anderson, R.C., Bell III, J.F., Britt, D.T., Bruckner, J., Dreibus, G., Economou, T., Ghosh, A., Golombek, M.P., Greenwood, J.P., Johnson, J.R., Moore, H.J., Morris, R.V., Parker, T.J., Rieder, R., Singer, R., Wanke, H., 1999. Chemical, multispectral, and textural constraints on the composition and origin of rocks at the Mars Pathfinder landing site. J. Geophys. Res. 104, 8679–8715.

Mishchenko, M.I., Dlugach, J.M., Yanovitskij, E.G., Zakharova, N.T., 1999. Bidirectional reflectance of flat, optically thick particulate layers: an efficient radiative transfer solution and applications to snow and soil surfaces. J. Quant. Spectrosc. Rad. Transfer 63, 409–432.

Murchie, S., Kirkland, L., Erard, S., Mustard, J., Robinson, M., 2000. Near-infrared spectral variations of martian surface materials from ISM imaging spectrometer data. Icarus 147, 444–471.

Mustard, J.F., Pieters, C.M., 1987. Quantitative abundance estimates from bidirectional reflectance measurements. Proc. Lunar Planet. Sci. Conf. 17, part 2, J. Geophys. Res. 92 (B4), E617–E626.

Mustard, J.F., Pieters, C.M., 1989. Photometric phase functions of common geologic minerals and applications to quantitative analysis of mineral mixture reflectance spectra. J. Geophys. Res. 94 (B10), 13619–13634.

Mustard, J.F., Li, L., He, G., 1998. Nonlinear spectral mixture modeling of lunar multispectral data: implications for lateral transport. J. Geophys. Res. 103 (E8), 19419–19425.

Nichols, T., Thomas, J., Kober, W., Velten, V., 1999. A comparison of quantitative techniques to discriminate mixed bidirectional laboratory reflectance spectra. In: SPIE Conf. on Algorithms for Multispectral and Hyperspectral Imagery V, vol. 3717, pp. 2–13.

Pinet, P.C., Boubault, F., Daydou, Y., Chevrel, S., 2000. Implementation of a laboratory wide field spectral imaging facility. In: EGS XXV General Assembly, Nice, France, April, 2000.

Pinet, P., Chevrel, S., 1990. Spectral identification of geological units on the surface of Mars related to the presence of silicates from Earth-based near-infrared telescopic charge-coupled device imaging. J. Geophys. Res. 95, 14435–14446.

Pinet, P.C., Cord, A., Daydou, Y., Boubault, F., Chevrel, S., Lapeyrere, V., 2001. Influence of linear versus nonlinear mixture on bidirectional reflectance spectra using a laboratory wide field spectral imaging facility. Lunar Planet. Sci. 32. Abstract 1552. Houston.

Pinet, P.C., Rosemberg, C., 2001. Regional photometry and spectral albedo of the eastern hemisphere of Mars in the 0.7–1 micron domain. Lunar Planet. Sci. 32. Abstract 1640. Houston.

Pinet, P.C., Cord, A.M., Chevrel, S., Daydou, Y., 2004. Optical response and surface physical properties of the lunar regolith at Reiner gamma formation from Clementine orbital photometry: derivation of the Hapke parameters at local scale. Lunar Planet. Sci. 35. Abstract 1660. Houston.

Poulet, F., Cuzzi, J.N., Cruikshank, D.P., Roush, T., Dalle Ore, C.M., 2002. Comparison between Shkuratov and Hapke scattering theories for solid planetary surfaces. Application to the surface composition of two Centaurs. Icarus 160, 313–324.

Poulet, F., Erard, S., 2004. Nonlinear spectral mixing: quantitative analysis of laboratory mineral mixtures. J. Geophys. Res. 109, E02009.

Roberts, D.A., Gardner, M., Church, R., Ustin, S., Sheer, G., Green, R.O., 1998. Mapping Chaparral in the Santa Monica mountains using multiple endmember spectral mixture models. Remote Sensing Environ. 65, 267–279.

Sabol, D.E. Jr., Adams, J.B., Smith, M.O., 1992. Quantitative subpixel spectral detection of targets in multispectral images. J. Geophys. Res. 97 (E2), 2659–2672.

Shepard, M.K., Arvidson, R.E., 1999. The opposition surge and photopolarimetry of fresh and coated basalts. Icarus 141, 172–178.

Shepard, M., Campbell, B., Bulmer, M., Farr, T., Gaddis, L., Plaut, J., 2001. The roughness of natural terrain: a planetary and remote sensing perspective. J. Geophys. Res. 106 (32), 777–796.

Shkuratov, Yu.G., Stankevich, D.G., 1992. The shadow effect for planetary surfaces with Gaussian mesotopography. Solar Syst. Res. 26, 201–211.

Shkuratov, Yu., Helfenstein, P., 2001. The opposition effect and the quasi-fractal structure of regolith: theory. Icarus 152, 96–116.

Shkuratov, Yu., Starukhina, L., Hoffman, H., Arnold, G., 1999. A model of spectral albedo of particulate surfaces: implications for optical properties of the Moon. Icarus 137, 235–246.

Shkuratov, Y.G., Stankevich, D.G., Petrov, D.V., Pinet, P.C., Cord, A.M., Daydou , Y.H., Chevrel, S.D., 2005. Interpreting photometry of regolith-like surfaces with different topographies: shadowing and multiple scattering. Icarus 173, 3–15.

Simonelli, D.P., Dodd, C., Veverka, J., 2001. Regolith variations on Io: implication for bolometric albedos. J. Geophys. Res. 106 (E12), 33241–33252.

Smith, M.O., Johnson, P.E., Adams, J.B., 1985. Quantitative determination of mineral types and abundances from reflectance spectra using principal components analysis, Proc. Lunar Planet. Sci. Conf. 15. J. Geophys. Res. 90, C797–C804. Supplement.

Stamnes, K., Tsay, S.C., Wiscombe, W., Jayaweera, K., 1988. Numerically stable algorithm for discrete-ordinate-method radiative transfer in multiple scattering and emitting layered media. Appl. Opt. 27, 2502–2509.

Stankevich, D., Shkuratov, Yu., 2000. The shadowing effect in regolith-type media: numerical modeling. Solar Syst. Res. 34, 285–294.

Stankevich D.G., Shkuratov Yu.G., 2004. Monte Carlo ray-tracing simulation of light scattering in particulate media with optically contrast structure. J. Quant. Spectrosc. Rad. Trans. In press.

Stankevich, D., Shkuratov, Yu., Muinonen, K., 1999. Shadow-hiding effect in inhomogeneous and layered particulate media. J. Quant. Spectrosc. Rad. Trans. 63, 445–458.

Stankevich, D., Shkuratov, Yu., Pinet, P.C., Cord, A.M., 2002. Light scatter by particulate surfaces with different types of topography. In: Solar System Remote Sensing Symposium, Pittsburgh, 2002, p. 81.

Stankevich, D., Shkuratov, Yu., Grynko, Ye., Muinonen, K., 2003. A computer simulation of multiple scattering of light rays in systems of opaque particles. J. Quant. Spectrosc. Radiat. Transfer 76, 1–16.

Tompkins, S., 2002. Unmixing the lunar surface. In: Solar System Remote Sensing Symposium, Pittsburg, 2002, pp. 87–88. LPI Contribution No.1129. Abstract.

Van de Hulst, H.C., 1980. Multiple Light Scattering. Academic Press, New York.